Vertical profiles of raindrop size distribution parameters of summer rainfall in the eastern Tibetan Plateau: retrieval method and characteristics

Pingyi Dong[1,2], Xingwen Jiang*[1,2], Xingbing Zhao[1,2], Yuanchang Dong[1,2], Jiafeng Zheng[3], Chun Hu[4], Guolu Gao[1,2], Lei Liu[5], Shulei Li[5], and Lingbing Bu[6]

[1] Heavy Rain and Drought-Flood Disasters in Plateau and Basin Key Laboratory of Sichuan Province, Institute of Tibetan Plateau Meteorology, China Meteorological Administration, Chengdu, 610072, China
[2] Institute of Plateau Meteorology, Chinese Academy of Meteorological Sciences, Beijing, 100081, China
[3] Chengdu University of Information Technology, Chengdu, 610072, China
[4] Sichuan Provincial Meteorological Observation and Data Centre, Chengdu, 610072, China
[5] National University of Defense Technology, Changsha, 410005 China
[6] Nanjing University of Information Science and Technology, Nanjing, 210044 China

Correspondence to: Xingwen Jiang (xingwen.jiang@yahoo.com)

Abstract. The eastern Tibetan Plateau has a high elevation, with a cold and dry atmospheric background. The features of the raindrop size distributions (DSD) in this region have notable differences from those in the plains. The general empirical relationships for retrieving parameters of precipitation from radar observations are not applicable in the eastern Tibetan Plateau. In this study, we developed a new method based on optimal estimation theory to retrieve the vertical profiles of N_0 and D_m from a Ka-band zenith-pointing Doppler radar. Validation by a field campaign during the summer of 2024 indicate that the average bias in the $\log_{10}(N_0)$ and D_m derived from the PARSIVEL[2] disdrometer and the retrieved values is 0.12 and -0.1 mm, demonstrating the effectiveness of the retrieved DSD parameters in this region. Based on the retrieved vertical profiles of DSD parameters, some unique characteristics are found. The heavy precipitation (the maximum value in the reflectivity profile exceeding 30 dBZ) exhibits a higher particle number concentration above 2 km and larger raindrop size in the bottom of the rainfall on average. The mean values of D_m above 2 km are approximately 0.5 mm, for heavy precipitation, the value increase as the raindrops fall, reaching a peak at around 0.5 km. Precipitation that occurs after the nighttime cooling usually has higher particle concentrations and smaller particle sizes. Based on the above research, empirical relationships for the quantitative precipitation estimates (QPE) and attenuation correction using Ka-band radar in the eastern Tibetan Plateau are established.

---

*Corresponding author : Xingwen Jiang

Email: xingwen.jiang@yahoo.com

1 Introduction

Modeling and forecasting of precipitation is one of the key challenges in the field of meteorology, with substantial
30   implications for quantifying the dynamics of water and energy cycles within the Earth-atmosphere system and improving the
accuracy of numerical weather and climate models (Maggioni and Massari, , 2019; Foufoula-Georgiou et al., 2020). The
parameters of raindrop size distributions (DSD) are critical for describing the microphysical processes during precipitation
(Thomas et al., 2021). Exploring the dynamic evolution of the vertical profile of DSD parameters may enhance the
understanding of precipitation processes (Tapiador et al., 2010). Also, DSD is associated with the backscattering signals of
35   radar observations, thereby affecting the outcomes of quantitative precipitation estimates (QPE) derived from radar (Gatidis
et al., 2022). Furthermore, DSD and their associated uncertainties are critical components of data assimilation systems and
numerical weather models (Yang et al., 2019).

The eastern Tibetan Plateau serves as a pivotal area for the transport of moisture from the Indian Ocean to eastern Asia (Xu
et al., 2019). The water cycle in this region affects precipitation patterns across China and the global climate (Hu et al., 2021).
40   The average altitude of this region is above 3000 m, and the atmospheric density is low, with a sparse water vapor content
(You et al., 2015). The unique atmospheric background in this region results in distinct features of DSD compared to plain
areas (Li et al., 2022). Exploring the characteristics of the vertical distribution of DSD parameters in the eastern Tibetan
Plateau is crucial for improving the accuracy of local microphysical parameterizations of precipitation and deepening the
understanding of the water cycle in this region.

45   The high temporal and spatial resolution of weather radar can provide continuous profiles of the precipitation parameters.
However, the precipitation intensity and the size of raindrops in the eastern Tibetan Plateau are relatively small compared to
those in the middle and lower reaches of the Yangtze River (Pu et al., 2021), and the sensitivity of weather radar to small
particles is limited. Ka-band radar exhibits superior spatial resolution and sensitivity to small precipitation particles, and has
been widely applied in the observation of precipitation microphysical parameter profiles (Clothiaux et al., 2007). Studies
50   have indicated that the attenuation of the reflectivity factor of Ka-band radar caused by large raindrops cannot be ignored
(Daisley and Aydin, 2002). To minimize the impact of the attenuation effect on the retrieval accuracy, the Doppler spectrum
observed by Ka-band radar was used to retrieve the parameters of DSD (Tridon and Battaglia, 2015; Giangrande et al., 2012).
However, the results may be affected by turbulence of air, and the retrieval may have multiple solutions (Williams et al.,
2016). Observations of the multi-frequency radar can provide additional information on the parameters of DSD. The dual-
55   frequency ratio and differential attenuation coefficients were used to constrain the retrieval of DSD parameters (Unal and
Van Den Brule, 2024; Hogan et al., 2005). Yet, the empirical relationships between the precipitation parameters and the
observations of radar were affected by the average features of DSD that were summarized from plain areas, and are therefore
not applicable in the eastern Tibetan Plateau (Protat et al., 2019). Further research is needed to accurately retrieve the
profiles of DSD parameters from Ka-band radar in the eastern Tibetan Plateau and to summarize the characteristics of the
60   vertical distribution of DSD in this region.

Due to the limited information obtained from single-frequency radar, the methods for retrieval of DSD parameters are generally chosen to fix the μ parameter of the Gamma Size Distribution (GSD) (Kumar et al., 2011) or utilize λ-μ empirical relationships of GSD to constrain the retrieval results (Huang et al., 2021). However, these assumptions inevitably introduce errors into the retrieval results. Although the GSD can provide a detailed structure of the DSD, previous studies have indicated that the Marshall–Palmer exponential (MP) drop size distribution is sufficient to represent the size distribution of particles for cloud liquid water and precipitation (Smith, 2003). Besides, the representation of rainfall in the weather and climate models usually adopts a single or two-parameter scheme for rainfall to reduce the complexity of calculation (Jin and Baik, 2023). This article presents a retrieval method developed for Ka-band zenith-pointing radar and the characteristics of retrieved vertical profiles of DSD parameters. The retrieval method is based on optimal estimation theory, corrects the precipitation attenuation layer by layer and retrieves the N_0 and D_m vertical profiles of MP distribution, and provides uncertainty estimates for the retrieval. This study primarily addresses the precipitation scenarios where the melting layer can be observed in radar LDR (Linear Depolarization Ratio) measurements. The retrieval and characteristics of DSD parameters under strong convective conditions are not included in this study. In section 2, the instruments and retrieval method used in this study are introduced. Section 3 presents the validations of the forward calculation and retrieval method. The spatiotemporal characteristics of the vertical profiles of the DSD parameters and the fitted empirical relationships are given in Section 4.

2 Instrument and retrieval method

During the 2024 summer precipitation observation experiment in the eastern Tibetan Plateau, a comprehensive study of cloud-precipitation was conducted at the Hongyuan Meteorological Bureau weather site (32.8°N, 102.5°E, 3499 m above sea level). In this study, the vertical distribution of DSD parameters of summer rainfall in the eastern Tibetan Plateau is investigated using a Ka-band zenith-pointing Doppler radar and a ground-based disdrometer deployed at the Hongyuan site. The distance between the two instruments is about 70 m.

2.1 Ground-based disdrometer

The surface DSD are collected by the PARSIVEL[2] disdrometer. The measuring ranges of the disdrometer are 0.062~24.5 mm for the size of raindrops and 0.05~20.8 m/s for the velocity, respectively. The time resolution is 60 s. According to the number of raindrops in the discrete scale intervals observed by the disdrometer *n* and the terminal falling velocity V, the raindrop size distribution *N(D)* in mm^{-1}m^{-3} is written as:

$$N(D_i) = \sum_{j=1}^{32} \frac{n_{i,j}}{A_i \cdot t \cdot V_{i,j} \cdot \Delta D_i} ,$$

(1)

Where $n_{i,j}$ represents the number of raindrops in the i-th size class and the j-th velocity class, A_i denotes the sampling area, t

90 is the integration time, and $V_{i,j}$ indicates the falling velocity of raindrops in the i-th size class and the j-th velocity class. The

particle diameter is expressed in millimeters (mm), while the velocity is measured in meters per second (m/s) in this study.

The MP exponential drop size distribution (Smith, 2003) expressed as:

$$N(D) = N_0 \exp(-\Lambda D) = N_0 \exp(-4D / D_m), \tag{2}$$

In Eq. (2), D is the maximum dimension of the particle, N_0 is the concentration parameter, mass-weighted mean diameter D_m,

95 determined as the ratio of the fourth to third moments of the DSD. N_0 are calculated from the third and fourth moments of

DSD (Smith, 2003), expressed as:

$$N_0 = 128 M_3^5 / (3 M_4^4) \tag{3}$$

The rain rate R is defined by the fall rate and DSD as:

$$R = \int n(D)(\pi D^3 / 6) V(D) \mathrm{d}D \tag{4}$$

100 For Ka-band radar, the Reflectivity factor (Z) in $mm^6 m^{-3}$ and the scalar radial velocity V_r are calculated from Eq. (5) and (6).

$$Z = \frac{\lambda^4}{\pi^5 |K|^2} \sum_{j=1}^{32} N(D_i) \sigma_b \Delta D_i = \frac{\lambda^4}{4\pi^4 |K|^2} \sum_{j=1}^{32} N(D_i) Q_b(D) D^2 \Delta D \tag{5}$$

$$V_r(D) = \frac{\int\limits_{D\min}^{D\max} N(D) V(D) \sigma_b \mathrm{d}D}{\int\limits_{D\min}^{D\max} N(D) \sigma_b \mathrm{d}D} \tag{6}$$

Where $|K|^2 \approx 0.88$. The backscattering section of radar σ_b and the extinction cross-section σ_e are calculated by

pyQuickBeam (Haynes et al., 2007), which is a software for calculating Mie scattering properties of spherical particles. In

105 Eq. 6, $V(D)$ is the final falling velocity of raindrops considering the correction term of altitude h (Atlas et al., 1973):

$$D = \frac{1}{0.6} \times \ln \frac{10.3}{9.65 - V(D) / \delta(h)} \tag{7}$$

$$\delta(h) = 1 + 3.68 \times 10^{-5} h + 1.71 \times 10^{-9} h^2$$

Historical observations of the disdrometer at Hongyuna site from June to August of 2021 to 2023 are used to obtain prior

information on the parameters of the MP size distribution of summer rainfall in this region. Based on the observed DSD, the

corresponding Z of Ka-band radar is calculated using Eq. (5). The calculated Z values are categorized into four intervals: [-

110 10,10), [10, 20], [20, 30), and [30, 45). The $\log_{10}(N_0)$ and D_m in each Z interval are counted separately. Approximately

113000 samples of DSD are collected. Figure 1 illustrates the box plots of the parameters of MP size distribution in different

intervals of Z. The results show that the distribution of the $\log_{10}(N_0)$ ranges from 1.0 to 5.6. The majority of D_m less than 1.7

mm. The statistical results indicate that as the Z of precipitation increases, the proportion of larger raindrops of DSD rises, and the concentration of raindrops decreases.
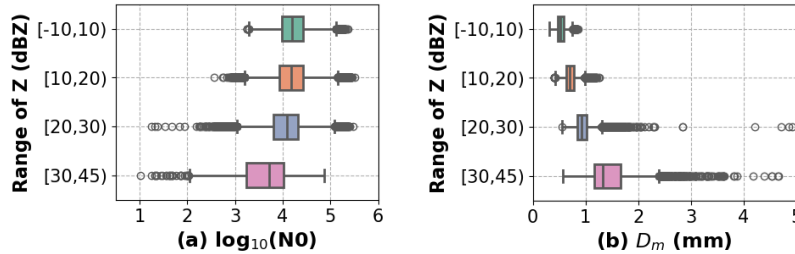
115 **Figure 1. Box plots of the parameters of MP size distribution in different Z intervals. (a) $\log_{10}(N_0)$. (b) D_m.**

2.2 Ka-band zenith-pointing observation radar

The Ka-band zenith-pointing radar operates at the frequency of 35 GHz. The observation uncertainties in the Z, V_r, and LDR are 0.5 dBZ, 0.5 m/s, and 0.5 dB, respectively. The detection range of radar is 0.12 to 20 km, with a vertical resolution of 30 m and a beam width less than 0.4°. The integration time is 60 s. To mitigate the impact of near-field uncertainties of radar

120 observations, the seventh range gate (180~210 m) of the radar is chosen as the first effective observation at the surface, denoted as h0. The "0" of h0 refers to the index of the range gate of the effective observations of radar. When the Z measured by radar at h0, Z_{h0}, exceeds -10 dBZ, it is identified as a precipitation scenario. The range gate of the precipitation height (htop) is determined from the bottom of the melting layer assessed by the LDR observations. The method (Thurai et al., 2016) for determining the htop is as follows:

$$LDR_{htop} > max([LDR_{h0},...,LDR_{h(top-1)}])$$
$$LDR_{htop} - LDR_{h(top-2)} >= 10 \text{ dB}$$

125   (8)

After determining the height of the precipitation layer, the parameters of the DSD are retrieved from bottom to top. For each range gate of the radar observation, the optimal estimation method is used to retrieve $\log_{10}(N_0)$ and Dm from Z and V_r. The optimal estimation is a widely used physical retrieval method that iterates the maximum probability state x_{op} of the parameters to be retrieved by combining observations, prior information, and associated uncertainties (Löhnert and Maier,

130 2012). The optimal estimation algorithm employed in this study is based on the publicly available code by Maahn et al. (Maahn et al., 2020). The observational vector y_{obs} of the optimal estimation algorithm consist of the Z and V_r observed by the Ka-band zenith-pointing radar. The first guess of the $\log_{10}(N_0)$ and D_m, x_a, and the covariance matrix S_a are set based on the prior information of the DSD in Hongyuan. The error covariance matrix S_y is set according to the observation uncertainty of Z and V_r. The x_a is taken as the input for Eq. (5) and (6) to calculate the simulated observation $F(x_a)$. The S_y and S_a are

135 then used to weight the difference of the $F(x_a)$ and y_{obs} for updating the x_a to x_{x+1}. The subscript is the iteration index. x_{x+1} is calculated by:

$$x_{x+1} = x_a + (S_a^{-1} + K_x^T S_y^{-1} K_x)^{-1} K_x^T S_y^{-1} [y - F(x_x, b) + K_x (x_x - x_a)] \tag{9}$$

Where K_x represents the Jacobian matrix computed at the x-th iteration, the iteration ceases when the result of the left side of Eq. (10) falls below the predetermined threshold χ.

140

$$(x_{x+1} - x_x)^T S_x^{-1} (x_{x+1} - x_i) = \chi \tag{10}$$

χ is typically set to the length of the parameters that are to be retrieved. S_x in Eq. (11) provides the uncertainty associated with the retrieved x_x:

$$S_x = (S_x^{-1} + K_x^T S_y^{-1} K_x)^{-1} \tag{11}$$

If the convergence of retrieval is achieved, the x_x and S_x are the optimal solution x_{op} and corresponding uncertainty S_{op}.

145 The retrieval process of the vertical profiles of the DSD parameters is described as follows. The temperature at Z_{h0} is set to 287.15 K based on statistical results of temperature from the microwave radiometer at a height of 210 m in Hongyuan. The temperatures at different range gates of the radar are calculated using the temperature lapse rate. The Z_{h0} is assumed to be unaffected by the attenuation effect. The Z_{h0} and V_{h0} are first contacted as the y_{obs} for the optimal estimation algorithm to retrieve the $\log_{10}(N_0)$ and D_m of the DSD at the surface. Then, the N_0 and D_m at the surface are used to correct the Z of the

150 next range gate $Z_{h(i+1)}$:

$$Z_{h(i+1)} = Za_{h(i+1)} \exp[-2\int_0^{h_i} k(h)dh] \tag{12}$$

where $Z_{h(i+1)}$ and $Za_{h(i+1)}$ are the attenuated and actual radar reflectivity in mm^{6}m^{-3}, k is the specific attenuation in dB/km, defined as:

$$k = \int_{Dmin}^{Dmax} \sigma_e N(D)dD = \int_{Dmin}^{Dmax} \frac{\pi D^2}{4} Q_e N(D)dD \tag{13}$$

155 Q_e is calculated from the drop size and temperature using the pyQuickBeam software. If the height of the following range gate, h(i+1), is less than htop, the observational vector of the next range gate is updated to $y_{obs\_h(i+1)} = [Za_{h(i+1)}, V_{h(i+1)}]$. Next, the optimal estimation is used to retrieve the $\log_{10}(N_0)$ and the D_m at h(i+1). Following this procedure, the observations of Z are corrected layer by layer, and the N_0 and D_m are retrieved bottom to top. The flowchart of the retrieval method is presented in Fig. 2.
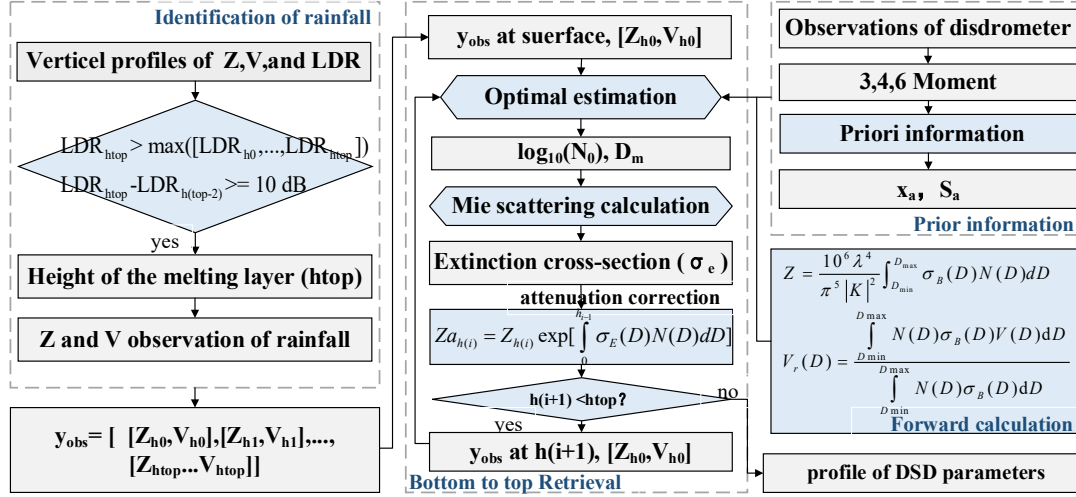
Figure 2. Flowchart for the retrieval method of vertical profiles of DSD parameters.

3 Validation

3.1 Validation of the forward calculation

The accuracy of forward calculations is crucial for the optimal estimation algorithm. The observations of the Ka-band zenith-pointing radar and the disdrometer during the field campaign are used to validate the forward calculations. The Z and V_r observed by the radar at h0 serve as the truth values, while the $N(D)$ observed from the PARSIVAL[2] disdrometer is used as the input to Eq. (5) and (6) to calculate the simulated Z and V_r. The mean error (ME), Pearson correlation coefficient (Pearson's r), and Jensen-Shannon divergence (JSD) are employed to assess the bias between the true values and the simulated values. The ME is used to evaluate the average difference between two datasets. Pearson's r measures the linear relationship between the two datasets. The JSD quantifies the similarity in the probability distributions of two datasets (Zhang et al., 2023).

Figure 3 illustrates the true values of Z and V_r observed from the Ka-band zenith-pointing radar and simulated values from the disdrometer during the field campaign in July and August 2024. According to the assessment metrics, the true values and the simulated values of Z and V_r are in good agreement. The ME of Z and V_r is 3.63 dBZ and -1.04 m/s. The Pearson's r of Z and V_r are above 0.88. For precipitation scenarios with $Z_{h0}<25$ dBZ, the Z calculated from the ground-based disdrometer observations generally exceeds the radar measurements. For radar observations with $Z≥25$ dBZ, the reflectivity factors derived from disdrometer measurements are typically lower than those observed by radar. The simulations and observations for V_r less than 3 m/s are consistent, while for V_r exceeding 3 m/s, the simulations tend to underestimate the values of V_r. JSD values of the simulated and observed suggest some mismatch in Z and V_r distributions. This is possibly due to
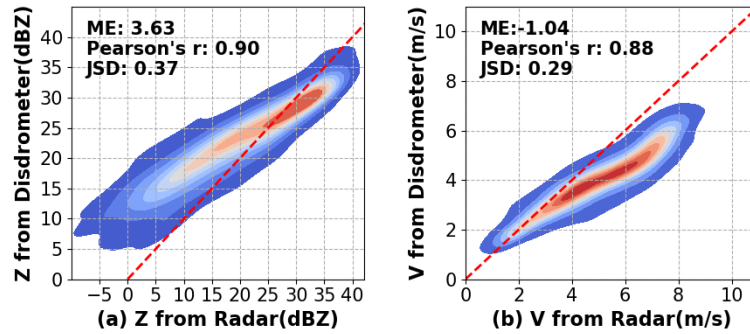
Figure 3. The true values of Z and V_r observed from the Ka-band zenith-pointing radar and simulated values during the field campaign in July and August 2024. (a) Z. (b) V_r.

3.2 Validation of the optimal estimation algorithm

185   To validate the effectiveness of the optimal estimation algorithm, a random stratified sampling of 1800 cases of DSD is selected from the historical observations of the ground-based disdrometers. Random noise within 0.5 dBZ and 0.5 m/s is added to the values of Z and V_r, which are calculated from the selected DSD cases with Eq. (5) and (6). Then the Z and V_r are taken as the input for the optimal estimation algorithm to retrieve the $\log_{10}(N_0)$ and D_m of DSD. The $\log_{10}(N_0)$ and D_m derived from the selected DSD with Eq. (3) are taken as the true values of the retrievals. The comparison of the retrieved values and the true values of $\log_{10}(N_0)$ and D_m is presented in Fig. 4. The average bias of the retrieved $\log_{10}(N_0)$ and D_m is -

190   0.056 and 0.015 mm, with the average uncertainties of 0.41 and 0.15 mm. The correlation between the retrieved values and the true values of $\log_{10}(N_0)$ and D_m both exceeds 0.9. The JSD values of 0.08 and 0.16 indicate a good consistency between the distributions of the retrieved values and the true values of $\log_{10}(N_0)$ and D_m. The source of the retrieval errors may be attributed to the random noise added to the Z and V_r. Furthermore, the errors of the retrieval are primarily observed in

195   scenarios where the D_m values exceeded 2.5 mm and the $\log_{10}(N_0)$ value is less than 2.6. This may be attributed to the lack of prior information in these cases.
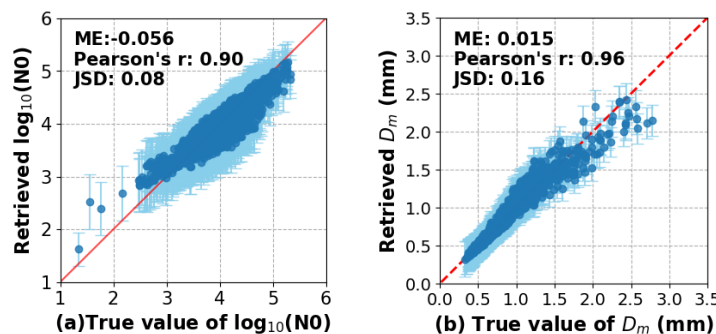
Figure 4. The retrieved values and the true values of $\log_{10}(N_0)$ and D_m. (a) $\log_{10}(N_0)$. (b) D_m.

The optimal estimation algorithm is further validated with the observations from the Ka-band zenith-pointing radar and the ground-based disdrometer in Hongyuan during the field campaign in July and August 2024. The Z and V_r observed by radar at h0 are used as inputs for the optimal estimation algorithm. The $\log_{10}(N_0)$ and D_m derived from the disdrometer are used for the comparison. Approximately 5900 effective observations of the radar and the disdrometer of precipitation are used for the validation. In Fig. 5, the retrieved values from the optimal estimation algorithm are denoted with black points, while the uncertainties of the retrieval are indicated by error bars in gray. The parameters of DSD derived from the disdrometer observations are marked with blue points. The correlation coefficients between the retrieved and the derived $\log_{10}(N_0)$ and D_m are 0.63 and 0.76. The ME of the retrieved and the derived $\log_{10}(N_0)$ and D_m are 0.12 and -0.01 mm, and average uncertainties are 0.41 and 0.16 mm, respectively. Most of the $\log_{10}(N_0)$ and D_m values derived from the disdrometer are within the uncertainty range of the retrievals. The JSD values indicate that the retrieved D_m values are consistent with the distribution of the observations of the ground-based disdrometer. The bias between the retrieved and observed parameters of DSD may be attributed to the observation uncertainties and the differences in the sampling volumes of the two instruments, as well as errors introduced during the fitting of parameters from DSD.
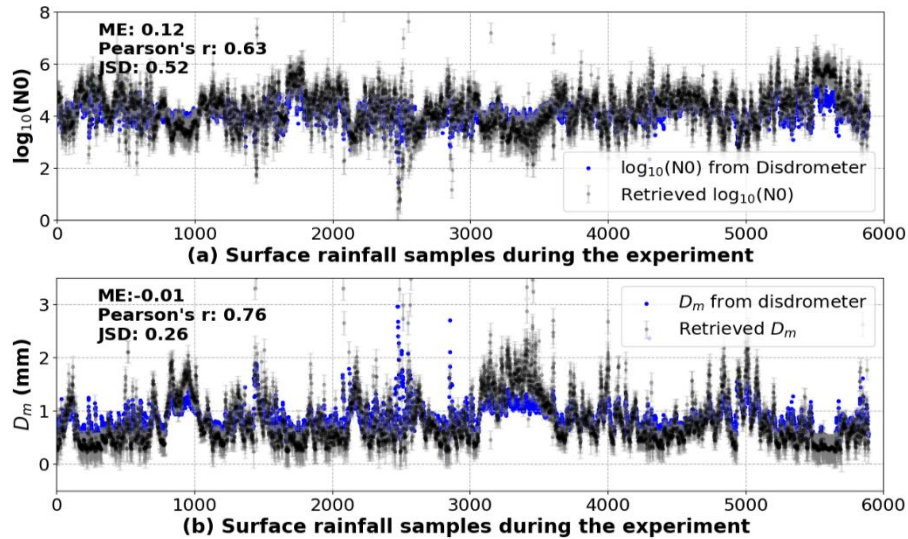
Figure 5. The retrieved and observed $\log_{10}(N_0)$ and D_m during the field campaign in July and August 2024. (a) $\log_{10}(N_0)$. (b) D_m.

4 Results

4.1 Case analysis

Figure 6 presents the attenuation-corrected profiles of Z for the precipitation on August 15, 2024, along with the retrieved vertical profiles of DSD parameters. The path-integrated attenuation (PIA) is also plotted in the figure. The precipitation

events occurred from CST 00:00 to 08:12 and from CST 10:08 to 12:04, totaling 517 minutes. The retrieved profile of DSD parameters demonstrates a close correlation with the process of precipitation. According to the profiles of Z, the height of the melting layer increased around the 110th to 120th samples of precipitation, with echo intensity exceeding 35 dBZ, indicating

220   potential convective activity accompanying the precipitation. The vertical variation of the retrieved N_0 and D_m is larger compared to other precipitation samples. The retrieved profiles of $\log_{10}(N_0)$ suggest a higher raindrop concentration in the upper levels of precipitation. The retrieved profiles of D_m indicate the presence of raindrops larger than 1.4 mm in both the upper and lower levels of precipitation. Samples 480 to 500 occurred at the end of a brief rainfall in the morning. The maximum value of Z is below 20 dBZ. The retrieved profiles of $\log_{10}(N_0)$ were generally larger than those of other

225   precipitation samples, while the retrieved profiles of D_m indicated smaller raindrop sizes. Based on the calculated PIA and the retrieved D_m profiles, the attenuation is attributed to larger-sized raindrops, with more than 2.6 dB/km of attenuation observed in the upper levels of the convective precipitation.
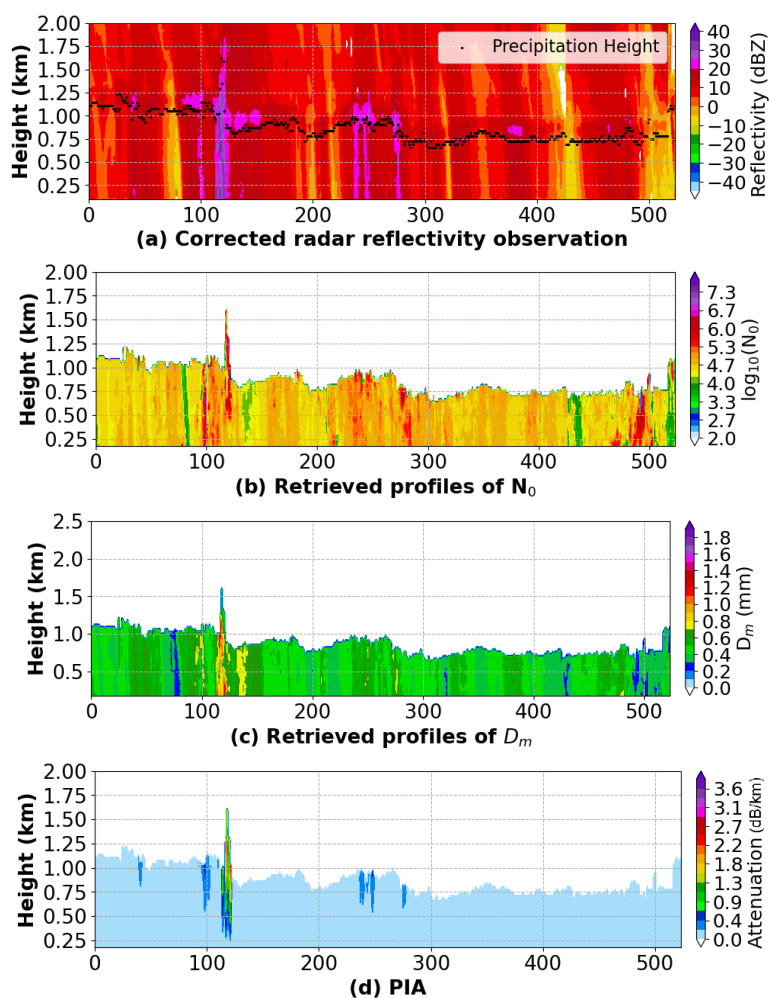
Figure 6. Profiles of the attenuation-corrected Z, the retrieved profiles of DSD parameters, and PLA of the precipitation on August 15, 2024. (a) Z. (b) $\log_{10}(N_0)$. (c) D_m and (d) PIA.

4.2 Characteristics of the vertical profiles of DSD parameters

Figure 7 presents the distribution and the mean values of DSD parameters with height during July to August 2024 at Hongyuan. The maximum value of the profiles of Z is used as the indicator of the heavy precipitation. If the indicator is larger than or equal to 30 dBZ, the precipitation sample is identified as heavy precipitation. As shown in Fig. 7 (a), the mean values of the $\log_{10}(N_0)$ for heavy precipitation are notably higher above 2 km, indicating a larger particle concentration at higher altitudes of heavy precipitation. At altitudes below 1.9 km, the mean values of the $\log_{10}(N_0)$ are lower than those of other lighter precipitation. This is consistent with the prior information that the particle concentration is lower in heavy precipitation. The mean values of $\log_{10}(N_0)$ and D_m for lighter precipitation show vertical variation. According to the statistical results for the D_m parameter, the mean values of D_m for both heavy and lighter precipitation above 2 km are approximately 0.5 mm. This may suggest that raindrops begin to detach from the cloud layer (Barthazy et al., 1998). The mean D_m for heavy precipitation is generally larger than lighter precipitation, and increases as the raindrops fall, reaching a peak at around 0.5 km. This may relate to the breakup effects of raindrops during their falling process. Based on an investigation on raindrop size vertical distribution at Tsukuba, Japan (Kobayashi and Adachi, 2001), a high number of giant raindrops appeared at an altitude of 3.25 km, and disappeared at altitudes below 2.75 km. In the eastern Tibetan Plateau, the breakup height of large raindrops is lower, which may be related to the lower atmospheric and convective boundary layer.
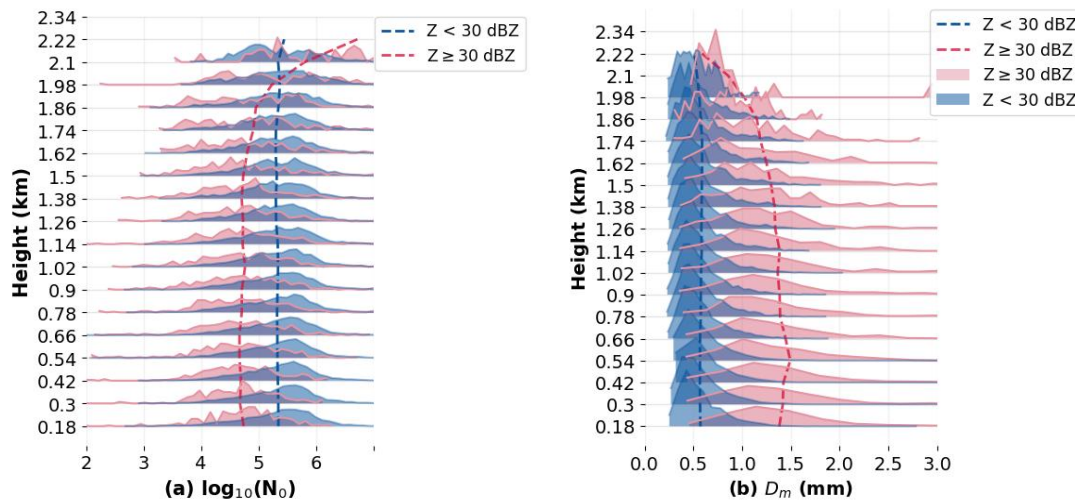
Figure 7. The distribution and the mean values of DSD parameters with height during July to August 2024 at Hongyuan. (a) $\log_{10}(N_0)$. (b) D_m.

Figure 8 presents the diurnal distribution of DSD parameters at heights of 210, 500, and 2000 m. The daytime in the Hongyuan region is longer than the nighttime in summer. The sunrise occurs around 6:20 in the morning, and the sunset

around 20:30. Usually, the precipitation intensity in this area in the afternoon is higher than that after the cooling at nighttime

250 (Liu and Yin, 2001). The broader distribution for the $\log_{10}(N_0)$ and D_m parameters exhibits around 17:00, likely associated with the convective precipitation that occurs during the afternoon. The mean value of the $\log_{10}(N_0)$ parameter at three different heights between 12:00 and 22:00 is lower than other times. This may relate to prior information on the DSD, which suggests that heavy precipitation typically has lower $\log_{10}(N_0)$ values. The D_m have larger mean values between 13:00 and 24:00 at three different heights, indicating that the sizes of raindrops are generally smaller during the nighttime. This is

255 consistent with the previously summarized features of DSD of lighter precipitation.

Compared with the lower reaches of the Yangtze River and the precipitation centers in South China, the melting layer of summer rainfall in the eastern Tibetan Plateau is lower, distributed from 0.72 to 2.1 km. The mean value of D_m is approximately 0.6-1.0 mm smaller (Huo et al., 2019; Li et al., 2024). Due to the differences in the features of the DSD parameters in the eastern Tibetan Plateau, empirical relationships for Z-R and D_m_R for QPE using Ka-band radar

260 during summer days and nights are fitted, as shown in Fig. 9 (a) and (b). According to the fitted empirical relationships, for the same value of R, the proportion of large raindrops in daytime precipitation is higher. Additionally, the Z-A relationship as well as the D_m-A/Z relationship that applied for single-frequency Ka-band radar to retrieve the precipitation parameters are fitted, as depicted in Fig. 9 (c) and (d). The fitted coefficients of the Z-A and the D_m-A/Z relationship in the eastern Tibetan Plateau are compared with the empirical relationships obtained from the OceanRAIN database at all latitudes (Protat

265 et al., 2019). The results indicate that for a measured Z, the specific attenuation is smaller, which is consistent with the smaller raindrop size in the eastern Tibetan Plateau.
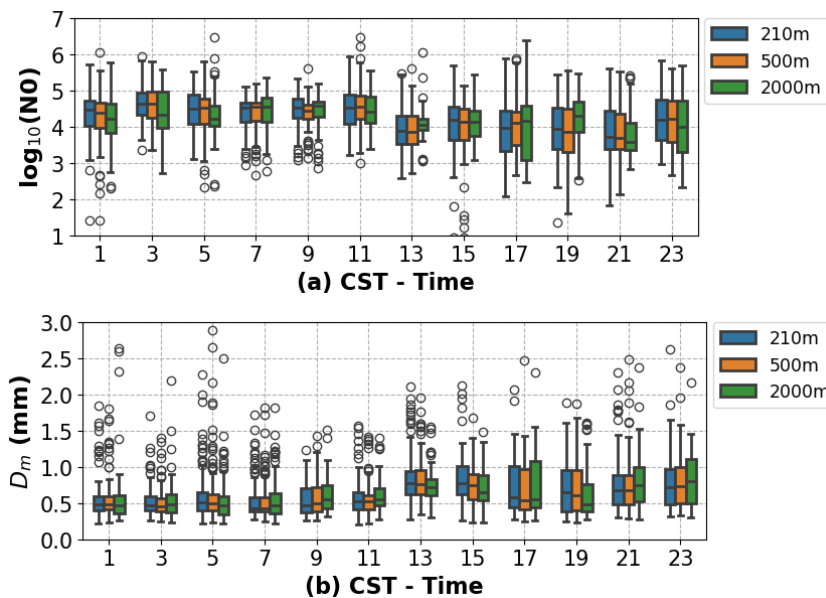
Figure 8. Box plots of the DSD parameters at 210, 500, and 2000 m. (a)N_0. (b)D_m.
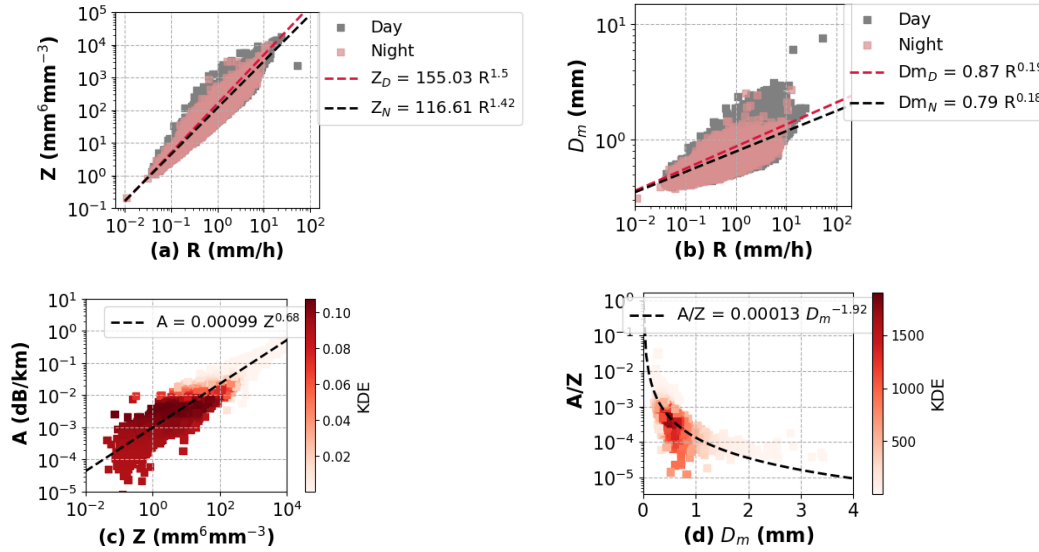
Figure 9. Empirical relations for QPE and attenuation correction using Ka-band radar in the eastern Tibetan Plateau. (a) Z-R relation. (b) D_m-R relation, (c) Z-A relation. (d) D_m-A/Z relation, where A refers to the specific attenuation in dB/km, Z in $mm^6 m^{-3}$.

5 Conclusion

Using observations from the Ka-band zenith-pointing Doppler radar and the ground-based disdrometer deployed in Hongyuan, the spatiotemporal characteristics of the vertical profiles of DSD parameters in the eastern Tibetan Plateau during summer are studied. A method based on optimal estimation theory is developed for retrieving the vertical profiles of DSD parameters from a Ka-band zenith-pointing radar. The method corrects the attenuation layer by layer, and retrieves the $\log_{10}(N_0)$ and D_m of the precipitation layer from bottom to top. The uncertainty estimation for the retrieval is provided based on the optimal estimation theory. The effectiveness of the optimal estimation algorithms is demonstrated using approximately 5900 synergistic observations from the disdrometer and the Ka-band zenith-pointing radar during the field campaign in the summer of 2024. The average bias of the $\log_{10}(N_0)$ derived from the ground-based disdrometer and the retrieved values from radar observations is 0.12, while the average bias in D_m is -0.01 mm, most of the values observed by the disdrometer falling within the uncertainty range of the retrievals.

According to the retrieved vertical profiles of DSD parameters, the heavy rainfall in this region has higher particle concentration above 2.0 km and a larger particle size at all heights on average. The mean values of D_m are approximately 0.5 mm above 2.0 km. For heavy precipitation, the particle size increases as the raindrops fall, reaching a peak at around 0.5 km. At the bottom of the heavy rainfall, the mean $\log_{10}(N_0)$ is lower than that of lighter precipitation, which is consistent with the prior information derived from the ground-based disdrometers.

In Hongyuan, heavy precipitation primarily occurs between 13:00 and 23:00 CST. During this period, the mean value of $\log_{10}(N_0)$ is lower, and D_m is larger. A broader distribution of the $\log_{10}(N_0)$ and D_m is observed around 17:00, likely associated with the convective precipitation that occurs during the afternoon. The precipitation after nighttime cooling generally has smaller particle sizes and higher particle number concentrations.

To enhance the accuracy of quantitative precipitation estimation and radar retrieval algorithms in the eastern Tibetan Plateau, Z-R and D_m-R relationships suitable for both daytime and nighttime conditions are fitted. In addition, to improving the accuracy of precipitation parameter retrieval using Ka-band radar in the eastern Tibetan Plateau, Z-A and the D_m-A/Z relationship are fitted. The parameter features of the fitted empirical relationships are consistent with the smaller raindrop size observed in the eastern Tibetan Plateau.

Due to the limited information provided by the single-frequency Ka-band radar, this study employed the M-P drop size distribution to avoid the errors introduced by the assumptions and empirical relationships of the GMD in the retrievals. Further evaluation is required to assess the impact of parameterizing the DSD on retrieval accuracy. In addition, the retrievals and characteristics under convective conditions are not considered; further research is necessary regarding the application of Ka-band zenith-pointing radar in these scenarios.

Data Availability Statement

Data and code are available at Zenodo: https://doi.org/10.5281/zenodo.15827786. The repository includes the processed datasets and Python scripts necessary to reproduce the figures and results presented in this paper. Access requests of raw data can be submitted to http://124.70.110.235:9091/SubPlat_ChengDu/.

Acknowledgments

This work has been supported by the National Key Research and Development Program of China under Grant 2023YFC3007501, the Sichuan Science and Technology Program under Grant 2025YFNH0006 and the Sichuan Provincial Central Leading Local Science and Technology Development Project under Grant 2024ZYD0175.

Author contributions

Conceptualization, PD and XJ; methodology PD, XJ, JZ, and GG; project administration, XJ, XZ and YD; writing—original draft preparation, PD; writing—review and editing XJ, CH, LL, SL, and LB; funding acquisition, JX and YD. All the authors contributed to the discussion.

Conflicts of Interest

The authors declare no conflict of interest.

315 **References**

Atlas, D., Srivastava, R., and Sekhon, R. S.: Doppler radar characteristics of precipitation at vertical incidence, Reviews of Geophysics, 11, 1-35, https://doi.org/10.1029/RG011i001p00001, 1973.

Barthazy, E., Henrich, W., and Waldvogel, A.: Size distribution of hydrometeors through the melting layer, Atmospheric research, 47, 193-208, https://doi.org/10.1016/S0169-8095(98)00065-9, 1998.

320 Clothiaux, E., Miller, M., Albrecht, B., Stephens, G., and Ackerman, T.: Millimeter-wavelength radars: New frontier in atmospheric cloud and precipitation research, Bulletin of the American Meteorological Society, 88, 1608-1624, https://doi.org/10.1175/BAMS-88-10-1608, 2007.

Daisley, S. E. and Aydin, K.: Relationships between rainfall rate, attenuation, and reflectivity at 14 and 35 GHz frequencies, IEEE International Geoscience and Remote Sensing Symposium, 2009-2011, 325 https://doi.org/10.1109/IGARSS.2002.1026429,

Foufoula-Georgiou, E., Guilloteau, C., Nguyen, P., Aghakouchak, A., Hsu, K.-L., Busalacchi, A., Turk, F. J., Peters-Lidard, C., Oki, T., and Duan, Q.: Advancing precipitation estimation, prediction, and impact studies, Bulletin of the American Meteorological Society, 101, E1584, https://doi.org/10.1175/bams-d-20-0014.1, 2020.

Gatidis, C., Schleiss, M., and Unal, C.: Sensitivity analysis of DSD retrievals from polarimetric radar in stratiform rain based 330 on the μ–Λ relationship, Atmospheric Measurement Techniques, 15, 4951-4969, https://doi.org/10.5194/amt-15-4951-2022, 2022.

Giangrande, S. E., Luke, E. P., and Kollias, P.: Characterization of vertical velocity and drop size distribution parameters in widespread precipitation at ARM facilities, Journal of Applied Meteorology and Climatology, 51, 380-391, https://doi.org/10.1175/JAMC-D-10-05000.1, 2012.

335 Haynes, J. M., Marchand, R. T., Luo, Z., Bodas-Salcedo, A., and Stephens, G. L.: A multipurpose radar simulation package: QuickBeam, Bulletin of the American Meteorological Society, 88, 1723-1728, https://doi.org/10.1175/BAMS-88-11-1723, 2007.

Hogan, R. J., Gaussiat, N., and Illingworth, A. J.: Stratocumulus liquid water content from dual-wavelength radar, Journal of Atmospheric and Oceanic Technology, 22, 1207-1218, https://doi.org/10.1175/JTECH1768.1, 2005.

340 Hu, X., Yuan, W., and Yu, R.: The extraordinary rainfall over the eastern periphery of the Tibetan Plateau in August 2020, Advances in Atmospheric Sciences, 38, 2097-2107, https://doi.org/10.1007/s00376-021-1134-7, 2021.

Huang, C., Chen, S., Zhang, A., and Pang, Y.: Statistical characteristics of raindrop size distribution in monsoon season over South China Sea, Remote Sensing, 13, 2878, https://doi.org/10.3390/rs13152878, 2021.

Huo, Z., Ruan, Z., Wei, M., Ge, R., Li, F., and Ruan, Y.: Statistical characteristics of raindrop size distribution in south 345 China summer based on the vertical structure derived from VPR-CFMCW, Atmospheric Research, 222, 47-61, https://doi.org/10.1016/j.atmosres.2019.01.022, 2019.

Jin, H. G. and Baik, J. J.: Do Double-Moment Microphysics Schemes Make Reliable Predictions on the Raindrop Number Concentration?: A Squall-Line Case Study, Journal of Geophysical Research: Atmospheres, 128, e2022JD038394, https://doi.org/10.1029/2022JD038394, 2023.

350 Kobayashi, T. and Adachi, A.: Measurements of raindrop breakup by using UHF wind profilers, Geophysical Research Letters, 28, 4071-4074, https://doi.org/10.1029/2001GL013254, 2001.

Kumar, L. S., Lee, Y. H., and Ong, J. T.: Two-parameter gamma drop size distribution models for Singapore, IEEE Transactions on Geoscience and Remote Sensing, 49, 3371-3380, https://doi.org/10.1109/TGRS.2011.2124464, 2011.

Li, M., Bi, Y., Shen, Y., Wang, Y., Nima, C., Chen, T., and Lyu, D.: Microphysical Characteristics of Rainfall Based on 355 Long-Term Observations with a 2DVD in Yangbajain, Tibet, Advances in Atmospheric Sciences, 41, 1721-1734, https://doi.org/10.1007/s00376-024-3299-3, 2024.

Li, Q., Wei, J., Yin, J., Qiao, Z., Cao, J., and Shi, Y.: Microphysical characteristics of raindrop size distribution and implications for radar rainfall estimation over the northeastern Tibetan Plateau, Journal of Geophysical Research: Atmospheres, 127, e2021JD035575, https://doi.org/10.1029/2021JD035575, 2022.

360 Liu, X. and Yin, Z.-Y.: Spatial and temporal variation of summer precipitation over the eastern Tibetan Plateau and the North Atlantic Oscillation, Journal of Climate, 14, 2896-2909, https://doi.org/10.1175/1520-0442(2001)014<2896:SATVOS>2.0.CO;2, 2001.

Löhnert, U. and Maier, O.: Operational profiling of temperature using ground-based microwave radiometry at Payerne: Prospects and challenges, Atmospheric Measurement Techniques, 5, 1121-1134, https://doi.org/10.5194/amt-5-1121-2012, 365 2012.

Maahn, M., Turner, D. D., Löhnert, U., Posselt, D. J., Ebell, K., Mace, G. G., and Comstock, J. M.: Optimal estimation retrievals and their uncertainties: What every atmospheric scientist should know, Bulletin of the American Meteorological Society, 101, E1512-E1523, https://doi.org/10.1175/BAMS-D-19-0027.1, 2020.

Maggioni, V. and Massari, C.: Extreme hydroclimatic events and multivariate hazards in a changing environment: a remote 370 sensing approach, Elsevier, 2019.

Protat, A., Klepp, C., Louf, V., Petersen, W. A., Alexander, S. P., Barros, A., Leinonen, J., and Mace, G. G.: The latitudinal variability of oceanic rainfall properties and its implication for satellite retrievals: 1. Drop size distribution properties, Journal of Geophysical Research: Atmospheres, 124, 13291-13311, https://doi.org/10.1029/2019JD031010, 2019.

Pu, K., Liu, X., Liu, L., and Gao, T.: Water vapor retrieval using commercial microwave links based on the LSTM network, 375 IEEE Journal of Selected Topics in Applied Earth Observations and Remote Sensing, 14, 4330-4338, https://doi.org/10.1109/JSTARS.2021.3073013, 2021.

Smith, P. L.: Raindrop size distributions: Exponential or gamma—Does the difference matter?, Journal of applied meteorology and climatology, 42, 1031-1034, https://doi.org/10.1175/1520-0450(2003)042<1031:RSDEOG>2.0.CO;2, 2003.

Tapiador, F., Checa, R., and De Castro, M.: An experiment to measure the spatial variability of rain drop size distribution 380 using sixteen laser disdrometers, Geophysical Research Letters, 37, https://doi.org/10.1029/2010GL044120, 2010.

Thomas, A., Kanawade, V. P., Chakravarty, K., and Srivastava, A. K.: Characterization of raindrop size distributions and its response to cloud microphysical properties, Atmospheric Research, 249, 105292, https://doi.org/10.1016/j.atmosres.2020.105292, 2021.

Thurai, M., Gatlin, P., and Bringi, V.: Separating stratiform and convective rain types based on the drop size distribution 385 characteristics using 2D video disdrometer data, Atmospheric Research, 169, 416-423, https://doi.org/10.1016/j.atmosres.2015.04.011, 2016.

Tridon, F. and Battaglia, A.: Dual-frequency radar Doppler spectral retrieval of rain drop size distributions and entangled dynamics variables, Journal of Geophysical Research: Atmospheres, 120, 5585-5601, https://doi.org/10.1002/2014JD023023, 2015.

390 Unal, C. and van den Brule, Y.: Exploring Millimeter-Wavelength Radar Capabilities for Raindrop Size Distribution Retrieval: Estimating Mass-Weighted Mean Diameter from the Differential Backscatter Phase, Journal of Atmospheric and Oceanic Technology, 41, 583-603, https://doi.org/10.1175/JTECH-D-23-0094.1, 2024.

Williams, C. R., Beauchamp, R. M., and Chandrasekar, V.: Vertical air motions and raindrop size distributions estimated using mean Doppler velocity difference from 3-and 35-GHz vertically pointing radars, IEEE Transactions on Geoscience 395 and Remote Sensing, 54, 6048-6060, https://doi.org/10.1109/TGRS.2016.2580526, 2016.

Xu, X., Dong, L., Zhao, Y., and Wang, Y.: Effect of the Asian Water Tower over the Qinghai-Tibet Plateau and the characteristics of atmospheric water circulation, Chinese Science Bulletin, 64, 2830-2841, https://doi.org/10.1360/TB-2019-0203, 2019.

Yang, Q., Dai, Q., Han, D., Chen, Y., and Zhang, S.: Sensitivity analysis of raindrop size distribution parameterizations in 400 WRF rainfall simulation, Atmospheric Research, 228, 1-13, https://doi.org/10.1016/j.atmosres.2019.05.019, 2019.

You, Q., Min, J., Lin, H., Pepin, N., Sillanpää, M., and Kang, S.: Observed climatology and trend in relative humidity in the central and eastern Tibetan Plateau, Journal of Geophysical Research: Atmospheres, 120, 3610-3621, https://doi.org/10.1002/2014JD023031, 2015.

Zhang, X., Delpha, C., and Diallo, D.: Performance evaluation of Jensen–Shannon divergence-based incipient fault diagnosis: 405 Theoretical proofs and validations, Structural Health Monitoring, 22, 1628-1646, https://doi.org/10.1177/14759217221111349, 2023.